PAPER

Check for updates

Density functional theory calculations for evaluation of phosphorene as a potential anode material for magnesium batteries

Xinpeng Han,[a] Cheng Liu,[a] Jie Sun, [ID] *[a] Austin D. Sendek [ID] [b] and Wensheng Yang [ID] [c]

We have systematically investigated black phosphorus and its derivative – a novel 2D nanomaterial, phosphorene – as an anode material for magnesium-ion batteries. We first performed Density Functional Theory (DFT) simulations to calculate the Mg adsorption energy, specific capacity, and diffusion barriers on monolayer phosphorene. Using these results, we evaluated the main trends in binding energy and voltage as a function of Mg concentration. Our studies revealed the following findings: (1) Mg bonds strongly with the phosphorus atoms and exists in the cationic state; (2) Mg diffusion on phosphorene is fast and anisotropic with an energy barrier of only 0.09 eV along the zigzag direction; (3) the theoretical specific capacity is 865 mA h g^{-1} with an average voltage of 0.833 V (*vs.* Mg/Mg^{2+}), ideal for use as an anode. Given these results, we conclude that phosphorene is a very promising anode material for Mg-ion batteries. We then expand our simulations to the case of bulk black phosphorus, where we again find favorable binding energies. We also find that bulk black phosphorous must overcome a structural stress of 0.062 eV per atom due to a volumetric expansion of 33% during magnesiation. We found that the decrease in particle size is good to increase its specific capacity.

1. Introduction

As one of the most successful means for electrochemical energy storage, Li-ion batteries (LIBs) power most of the electronic devices used in today's information-rich mobile society.[1] Recently, they have also been tested with success in hybrid, plug-in hybrid, and electric vehicles (EVs).[2] Moreover, as the integration of intermittent renewable energy on the electrical grid increases, the demand for large-scale, inexpensive and efficient energy storage systems is increasing accordingly.[3,4] However, LIBs are not ideal due to the high cost and scarcity of lithium. Sodium-ion batteries (SIBs)[5–7] and magnesium-ion batteries (MIBs)[8–11] have been proposed as potential alternatives for LIBs because of their low cost, large resources and availability, as shown in Table 1. While SIBs are attractive and are in fact already used for large-scale energy storage,[12,13] their low gravimetric and volumetric capacities mean they are not suitable for the applications which require high energy density, such as electric vehicles and portable electronics. On the other hand, MIBs are currently emerging as a viable next generation rechargeable battery technology,[9,10] with several companies in fact already working towards commercialization. MIBs have several advantages over LIBs and SIBs: (i) the divalent nature of the Mg ion results in the storage of up to two electrons per Mg atom *versus* only one for Li and Na, leading to a higher theoretical volumetric capacity, and a specific capacity comparable to those of Li; (ii) the atomic radius of Mg is smaller than Na and is comparable to Li, resulting in fast diffusion; and (iii) Mg can be electrodeposited rather smoothly without the dendrite formation problem[14–19] that plagues metallic Li and Na.

Most work on Mg batteries focuses on the development of cathode materials while simply using metallic Mg anodes.[10,20,21] Despite this work, the cycling abilities of MIBs remain poor. Much of this poor performance is rooted in problems with the reaction of Mg metal with electrolyte species, resulting in the formation of a passivating surface film[22,23] that inhibits any electrochemical reaction. In addition, electrode–electrolyte interactions also limit the achievable battery voltage.[23] Thus, identifying superior anode materials to Mg metal is a critical step in improving MIBs. Even though phosphorus has been

[a]School of Chemical Engineering and Technology, Tianjin University, Tianjin, China. E-mail: jies@tju.edu.cn

[b]Department of Applied Physics, Stanford University, Stanford, California 94305, USA

[c]State Key Laboratory of Chemical Resource Engineering, Beijing University of Chemical Technology, Beijing 100029, P. R. China

Table 1 Comparison of metallic Li, Na, and Mg anode for Li-, Na-, and Mg-ion batteries, respectively

	Li	Na	Mg
Ionic radius (pm)	128	166	141
Volumetric capacity (mA h cm^{-3})	2062	1130	3832
Gravimetric capacity (mA h g^{-1})	3830	1165	2205
Price ($ kg^{-1})	1500	300	35
Amount in Earth's crust	0.0065%	2.36%	2.33%

reported as attractive anode for LIBs[24–28] and SIBs,[29–34] the experimental and theoretical research has not focused on phosphorus as an anode for Mg-ion batteries.

When allowed to proceed to completion, phosphorus undergoes a conversion reaction with Mg to form Mg_3P_2, delivering a high theoretical specific capacity of 2596 mA h g^{-1} with a large volumetric expansion of 277%. As reported in experiments in LIBs and SIBs,[25,29] the breaking of P–P bonds upon reaction with Mg is very exothermic and difficult to reverse, resulting in a huge irreversible capacity. To solve these problems, we can use layer-structure black phosphorus as anode and stop the reaction after intercalation, which does not require the breaking of P–P bonds and has minimal volumetric expansion, thus allowing longer life cycling.

Here, we report the theoretical studies of two new candidates for MIB anodes: bulk black phosphorus and monolayer phosphorene,[35,36] which is exfoliated from black phosphorus. Although many important literatures about theoretical investigations of MIBs have been reported recently,[37–39] the theoretical research has not focused on black phosphorus as an anode for MIBs. We use DFT to analyze Mg adsorption and diffusion in both of these materials. We find that bulk black phosphorus and monolayer phosphorene can store Mg atoms via insertion and adsorption with a binding energy of −1.366 eV and −0.716 eV, respectively, which is larger than the binding energy of the Mg_2 dimer (−0.134 eV), indicating a strong interaction between Mg ion with phosphorene. The bulk and monolayer materials deliver a theoretical specific capacity of 433 and 865 mA h g^{-1}, respectively. Moreover, we find Mg diffusion in phosphorene shows a strong directional anisotropy because of the puckered structure, with fast Mg diffusion along the zigzag direction. Furthermore, our results reveal that the Mg storage in phosphorene and black phosphorus has good stability. Due to these factors, and the large active surface area and space available for Mg diffusion, we conclude phosphorene is a promising candidate for Mg-ion battery anodes.

2. Computational details

First-principles calculations are performed within the density-functional theory (DFT) framework, as implemented in CASTEP package[40,41] (in the Materials Studio version 5.5). The electron exchange and correlation interaction is described by the generalized gradient approximation (GGA) method using Perdew–Burke–Ernzerhof (PBE) pseudopotentials. The following valence electron configurations are used: P ($3s^2 3p^3$) and Mg ($2s^2 2p^6 3s^2$). After checking for convergence, 500 eV was chosen as the cut-off energy of the plane-wave basis for the Kohn–Sham states. All atomic positions and lattice vectors were fully optimized using a conjugate gradient algorithm to obtain the unstrained configuration. Atomic relaxation was performed until the change of total energy was less than 0.01 meV and all the forces on each atom were smaller than 0.01 eV Å^{-1}. For calculating the charge density difference between Mg atoms and phosphorene layer, the orbital calculations were performed in the DMol^3 package.

For the Mg adsorption and diffusion studies, we use a supercell containing 3 × 3 primitive cells of phosphorene, resulting in a Mg/P ratio of 0.028. We introduce a vacuum space of 25 Å between adjacent layers to avoid mirror interactions, and use 5 × 5 × 1 (monolayer phosphorene) and 5 × 5 × 5 (bulk black phosphorus) K-point meshes for the structure relaxation, denser meshes of 15 × 15 × 1 (monolayer) and 15 × 15 × 15 (bulk) for energy calculation, respectively. For Mg diffusion in phosphorene, we perform minimum energy path profiling using PBE method as implemented in the CASTEP transition state tools. The structural convergence criteria were similar to that used in the above-mentioned structure optimization.

3. Results and discussion

3.1. Adsorption of Mg on phosphorene surface

As illustrated in Fig. 1a, the Mg atoms are first loaded to phosphorene surface then diffuse along armchair or zigzag direction on the surface. As a consequence, we examine the surface loading (adsorption process) of an Mg atom on the phosphorene surface. We explore the phosphorene surface for Mg binding by placing one Mg atom at different sites above phosphorene before performing the structural relaxation and find that the most stable binding site is above the groove between two P "slifftops" as shown in Fig. 1b and c. Specifically, the distance between Mg and P1 atom is 2.731 Å, and the distances between Mg and the P2/P3 atoms is 2.881 Å. As an electrode material, it is essential for monolayer phosphorene to attract Mg with a relatively strong binding energy. The binding energy (E_b) can be evaluated with the following expression:

$$E_b = E_{total} - E_P - E_{Mg} \tag{1}$$

where E_{total}, E_P, and E_{Mg} are the total energy of Mg-adsorbed phosphorene, the energy of the phosphorene layer alone, and the energy of a Mg atom, respectively. According to this definition, a more negative value of E_b indicates a more energetically favorable (exothermic) reaction. From our calculation, the value of E_b for Mg on monolayer phosphorene is −0.716 eV, which is much larger than the Mg_2 dimer binding energy (−0.134 eV) and the binding energy of Mg on graphene (−0.005 eV). This indicates that incident Mg would be adsorbed on the surface of phosphorene, and that clustering of Mg atoms is unfavorable at low Mg concentration. Furthermore, the main crystal planes of Mg metal are (1 0 1), (0 0 2), (1 0 0) and (1 0 2), respectively. The binding energies of Mg atom loading on the above-mentioned specific Mg surfaces are −0.92 eV, −1.07 eV, −0.99 eV and −0.39 eV, respectively. Although the first three values are little higher than that of Mg atom loading on phosphorene (−0.716 eV), the reactive potential of Mg atom loading on Mg metal is 0 V (vs. Mg/Mg^{2+}) much lower than on phosphorene (average voltage, 0.833 V vs. Mg/Mg^{2+}). Thus, the former reaction cannot compete with the latter at the potential above 0 V vs. Mg/Mg^{2+}.

The spatial distribution of the charge difference between Mg and phosphorene is illustrated in Fig. 1d. The large charge
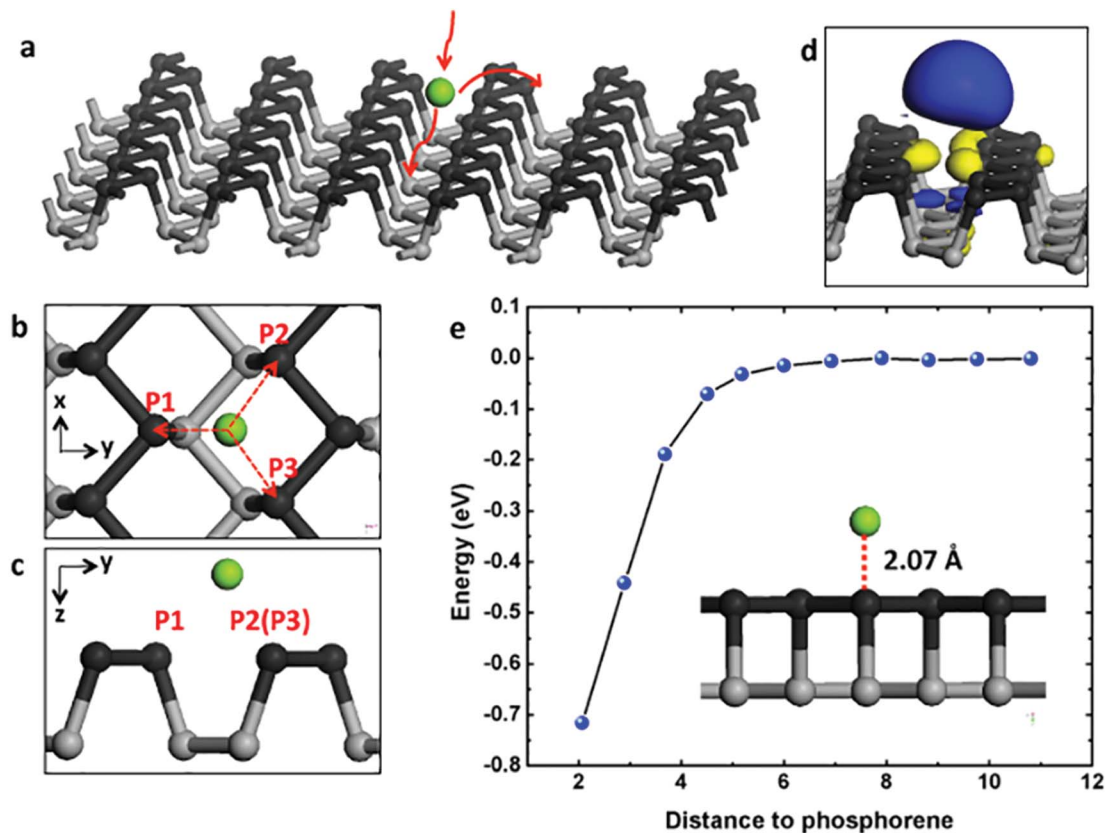
Fig. 1 (a) Schematic of Mg surface loading (adsorption process), diffusion along armchair and zigzag directions on phosphorene surface; (b) top view and (c) side view of the most stable binding site of Mg loading onto the monolayer phosphorene surface; (d) charge density difference between Mg and phosphorene, in which blue color means charge deficient and yellow color means charge sufficient; (e) total potential energy of Mg on phosphorene surface with respect to Mg–phosphorene distance.

deficiency at Mg and charge excess around nearby P atoms indicates strong electron transfer from Mg to phosphorene. According to Bader charge population analysis, Mg possesses a unit positive charge with its $3s^2$ electron being completely transferred to phosphorene and thus exists in the cationic state. To test the distance dependence of the binding energy, we move the Mg atom vertically away from the phosphorene surface, with the separation distance to the phosphorene surface running from 2.07 Å (the most stable binding site) to about 1.1 nm. The change of binding energy with respect to the Mg–phosphorene surface distance is shown in Fig. 1e. For distances larger than 7 Å, the energy is effectively zero. This means that beyond 7 Å the total energy of the complex system does not change because Mg has no interactions with phosphorene; it essentially can be treated as an isolated Mg atom and an isolated phosphorene sheet. Within about 5 Å, however, the energy decreases dramatically, indicating a strong attractive interaction between Mg and P atoms. It is clear that there is no energy barrier in the Mg loading process.

3.2. Diffusion of Mg on phosphorene surface

The charging and circuit rate performance of the MIBs is mainly determined by the Mg mobility on the electrode material. Hence it is desirable to quantify the diffusion of Mg on the surface of phosphorene. Distinct from the uniform sp^2 hybridization of C

atoms in graphene, phosphorene has a puckered structure with its atoms arranged in a honeycomb lattice when seen from the top view as shown in Fig. 1a–c. This structural anisotropy plays an important role in the migration of Mg atoms on its surface. Considering the symmetry of the primitive cell, there are only two unique (high-symmetry) paths connecting equilibrium sites. As illustrated in Fig. 2, these two diffusive pathways fall along the zigzag direction (Fig. 2a–c) and the armchair direction (Fig. 2d–f). Along the zigzag direction, the migration barrier is only 0.09 eV (in Fig. 2c), while for the armchair direction the barrier is 0.56 eV (in Fig. 2f). Thus Mg diffusion in phosphorene shows a strong directional anisotropy due to this puckered structure.

Compared with the previous study of Sn anode for Mg ion insertion,[42] the Mg diffusion barrier in α-Sn and β-Sn are 0.395 eV and 0.435 eV, respectively, which are much larger than the Mg diffusion barrier in phosphorene along the zigzag direction (0.09 eV). Another example, the Li diffusion barrier are 0.25 eV in MoS_2 and 0.327 eV in graphene,[43] respectively, which are much higher than 0.09 eV in phosphorene.

The temperature-dependent molecular transition rate can be evaluated by the Arrhenius equation from which the diffusion constant (D) of Mg follows:

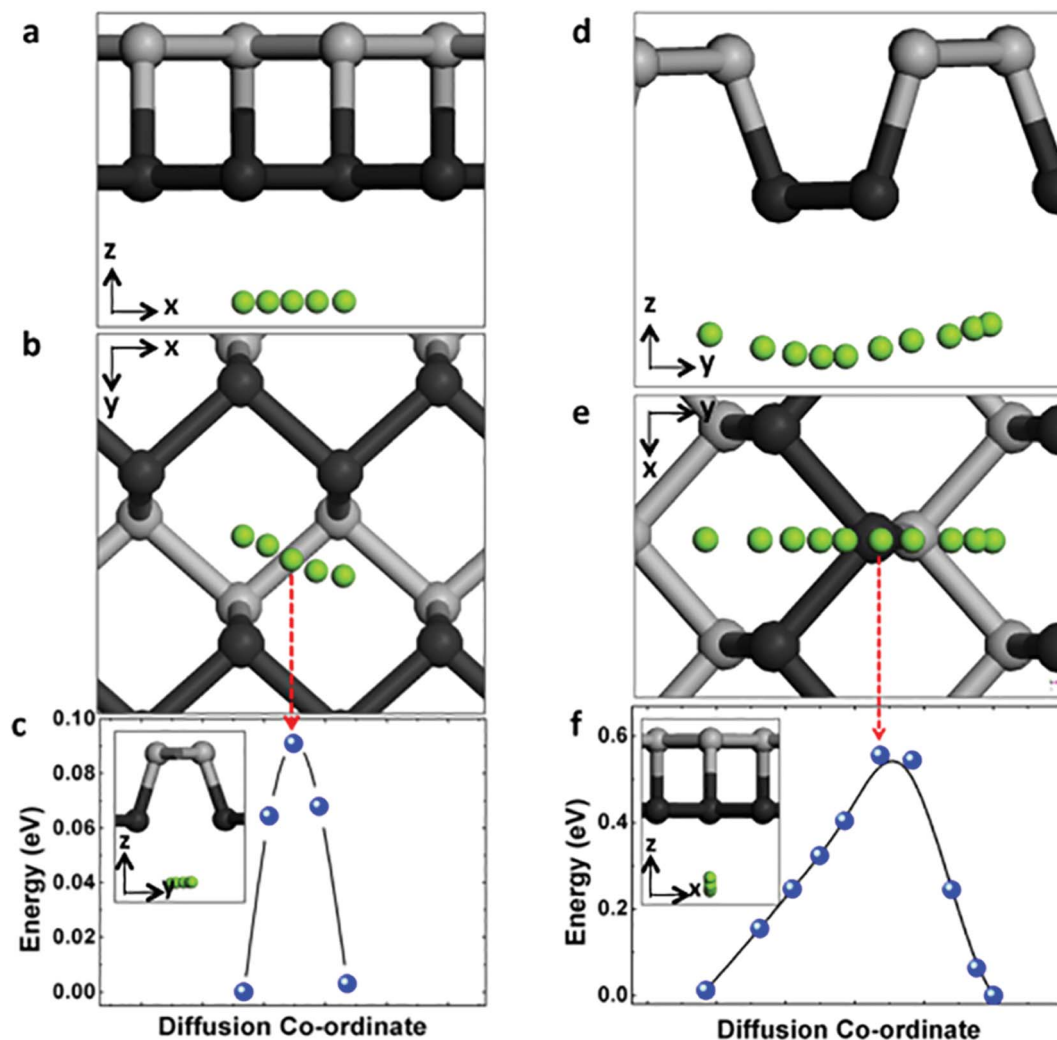$$D \sim \exp\left(\frac{-E_a}{k_B T}\right) \quad (2)$$

Fig. 2 (a) and (b) Schematic and (c) energy profiles of Mg diffusion along zigzag direction on phosphorene surface; (d) and (e) schematic and (f) energy profiles of Mg diffusion along armchair direction on phosphorene surface.

where E_a and k_B are the activation energy (diffusion barrier) and Boltzmann's constant, and T is the environmental temperature. According to eqn (2), the diffusion mobility of Mg along the zigzag direction of the phosphorene surface is 8.9×10^7 faster than that along the armchair direction at room temperature, indicating that without an external electrical field, the large energy barrier (0.56 eV) along the armchair direction essentially prevents Mg diffusion along this direction at room temperature. The binding position corresponding to the saddle point along the armchair path is labeled as a red arrow at the top of a P atom as shown in Fig. 2e and f. Hence the high diffusion barrier is due to the phosphorus "slifftop" between two adjacent grooves that makes the Mg diffusion extremely difficult. The remarkably quasi-one-dimensional Mg diffusion observed is similar to Li diffusion in monolayer phosphorene,[44] which is clearly absent in other 2D materials (e.g. MoS_2 and graphene). Amazingly, our calculations show that at room temperature the Mg diffusion mobility in phosphorene (zigzag direction) is estimated to be 7.6×10^6, 2.1×10^{10}, and 2.6×10^{15} times faster than that in

Sn, Ge and Si,[45] respectively. Therefore, an extremely high-rate capability is expected for phosphorene-based Mg-ion batteries.

3.3. Theoretical capacity and voltage profile of magnesiation in phosphorene

In this work, we consider a series of higher configurations with stoichiometry of Mg_xP ($x = 0.0278, 0.0556, 0.0833, 0.125, 0.25$ and 0.5), as shown in Fig. 3a, with one Mg atom binded on one side of a 3×3 supercell, two Mg atoms binded on one side of 3×3 supercell, three Mg atoms binded on one side of 3×3 supercell, two Mg atoms binded on one side of 2×2 supercell, one Mg atom binded on one side of 1×1 supercell, and two Mg atoms binded on the two sides of 1×1 supercell, respectively. We only consider Mg bonded on both sides of the phosphorene for the case of high Mg concentration, as we anticipate local electronic distortions fall of rapidly with distance and thus are unlikely to affect the total energy at low concentration – hence it should not matter what side of the layer the Mg is on. In the case of MgP_2, the reason why we set up the Mg atoms on both sides
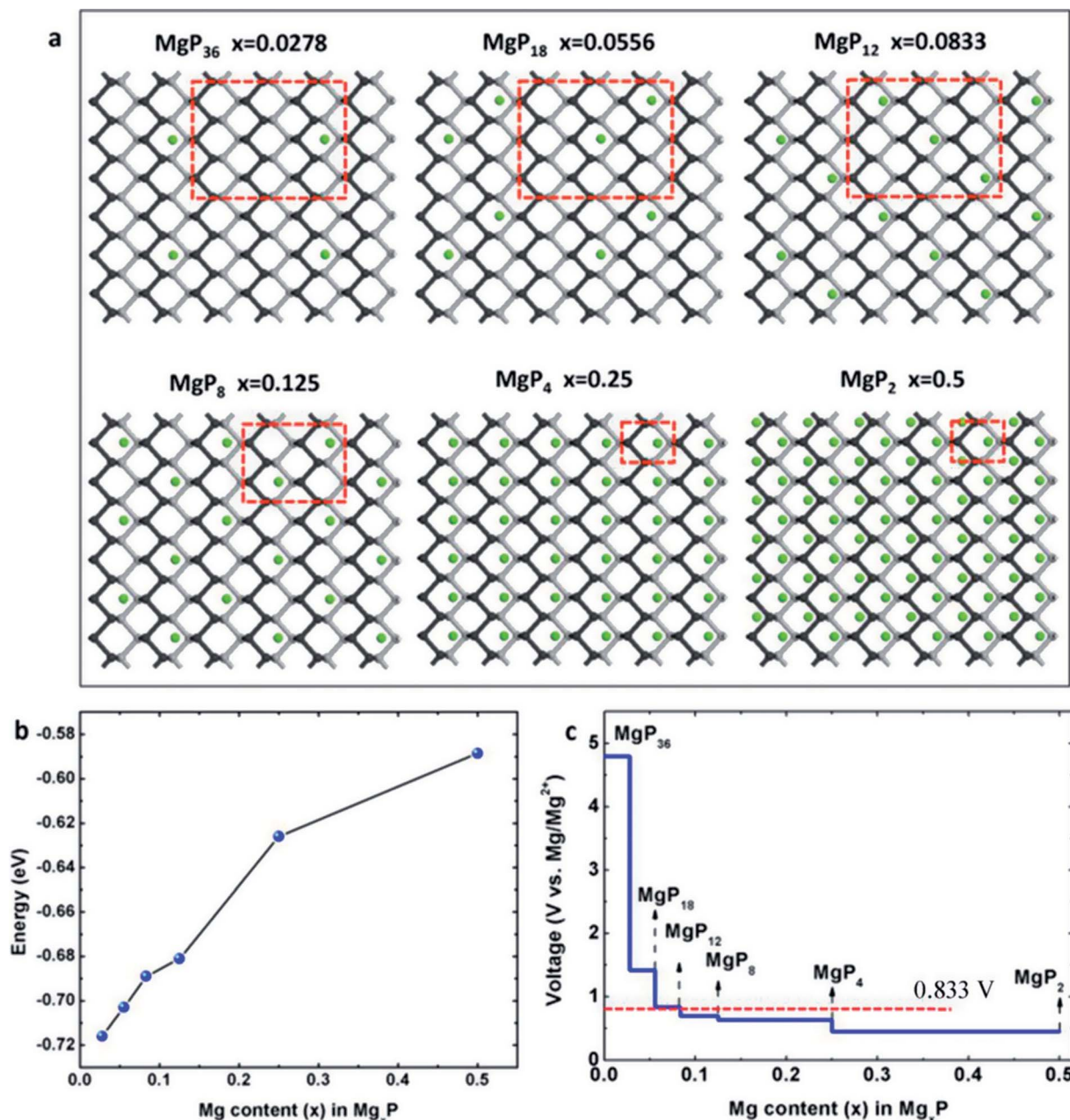
Fig. 3 (a) Configurations of schematics of Mg_xP with Mg binded on one side of phosphorene ($x = 0.0278–0.25$), and two side of phosphorene ($x = 0.5$); (b) binding energies with respect to Mg concentration; (c) calculated voltage profile with respect to Mg content from 0 to 0.5.

of phosphorene instead of just one side is analyzed in Fig. 4. The binding energy of MgP_2 with the Mg on two sides is −0.589 eV (Fig. 4c and d), slightly smaller than that of MgP_{36} (−0.716 eV). Compare this to a binding energy of 3.60 eV for MgP_2 with the Mg on one side (Fig. 4a and b); this positive value indicates a very difficult reaction. This instability can be attributed to the pronounced electrostatic repulsive interactions between adjacent Mg cations, which have a separation distance of 1.781 Å, much shorter than that in Mg metal (3.197 Å). Thus, forcing higher concentrations of Mg insertion into phosphorene (*i.e.* more than one Mg atom on one side of the primitive cell, $x > 0.5$) will cause P–P bond breaking, disrupting

the layered structure. As reported in the experiments in LIBs and SIBs,[25,29] the breaking of P–P bonds cannot be rebuilt and hence the lithiation/delithiation or sodiation/desodiation process becomes irreversible. As a consequence, we limit our consideration to Mg concentrations for which $x ≤ 0.5$, equal to a capacity of 865 mA h g^{-1}. The absolute value of the binding energy in Mg_xP decreases with increasing x. For all the concentrations (Fig. 3b), Mg has a binding energy lower than −0.59 eV. Notably, the slight discontinuity (from $x = 0.0833$ to 0.125) indicates that the complex becomes less stable due to the pronounced electrostatic repulsive interactions between
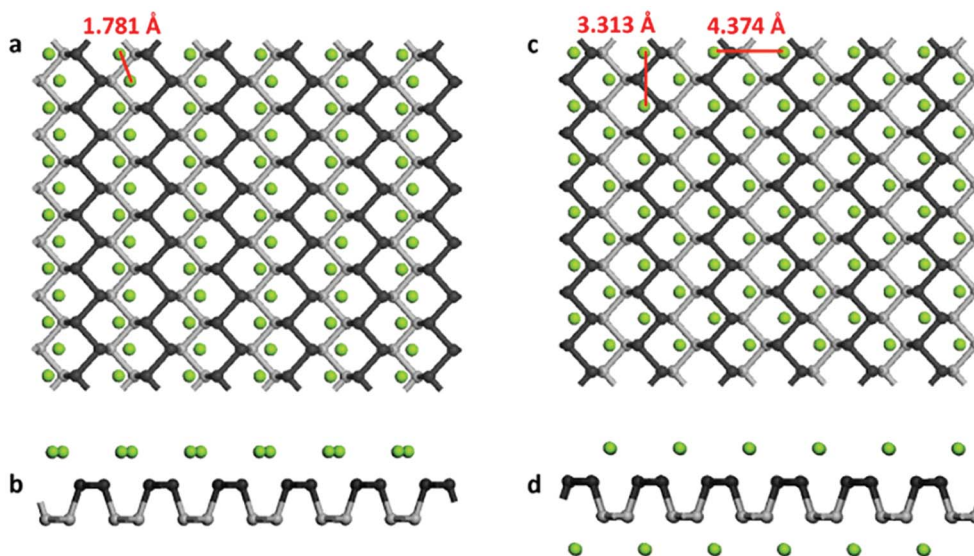
Fig. 4 (a) Top and (b) side views of the schematics of MgP_2 with Mg binded on one side; (c) top and (d) side views of the schematics of MgP_2 with Mg binded on two side.

adjacent Mg cations. This phenomenon also exists for lith-iation[44] and sodiation[46] in phosphorene.

Open-circuit-voltage data is widely used for characterizing the performance of batteries. In theory, the open circuit voltage curve can be obtained by calculating the average voltage over parts of the Mg composition domain. The average voltage of Mg_xP in the range of $x_1 \leq x \leq x_2$ is given as

$$V = \frac{-E(Mg_{x_2}P) - E(Mg_{x_1}P) - (x_2 - x_1)E(Mg)}{2(x_2 - x_1)e} \quad (3)$$

where $E(Mg_{x_1}P)$, $E(Mg_{x_2}P)$, and $E(Mg)$ are the energy of $Mg_{x_1}P$, $Mg_{x_2}P$, and metallic Mg, respectively, and e is the fundamental charge.[40,44,45] By using a series of Mg/P ratios (x values) for which we calculate the binding energy, the average insertion potential and the charge voltage profiles at these concentrations can be predicted; this is shown in Fig. 3c. There is a dramatic drop from 4.8 V when $x < 0.03$, and then the voltage profile becomes a gently sloping curve. The average voltage of the Mg storage in phosphorene is estimated to be 0.833 V ($vs.$ Mg/Mg^{2+}), suitable for the application as anode in MIBs.

3.4. Theoretical capacity of magnesiation in black phosphorus

We have also loaded Mg atoms into the interlayers of bulk black phosphorus by placing one Mg atom at different sites before structural optimization and found that the most stable binding site is as shown in the insert (at II state) of Fig. 5a. We note that this site is close to the equilibrium monolayer site but displaced slightly. For the case of Mg insertion into the interlayers of black phosphorus, the binding energy (E_b) can be evaluated as following

$$E_b = E_{total} - E_P - E_{Mg} \quad (4)$$

where E_{total}, E_P, and E_{Mg} are the total energy of Mg-intercalated bi-layer black phosphorus, the energy of bi-layer black phosphorus (from a black phosphorus crystal with an original interlamellar spacing of 3.07 Å), and the energy of a Mg atom, respectively. From our calculation, the value of E_b for Mg insertion in bi-layer black phosphorus is a very energetically unfavorable value of 2.676 eV when the original channel size is 3.07 Å.

However, in reality the layers will expand to accommodate the Mg atom. Thus we optimize the distance between the two phosphorene layers symmetrically around the Mg atom, with the interlayer channel size running from 3 Å to 6 Å. The change of binding energy with respect to channel size is shown in Fig. 5a. As the channel increases, the binding energy drops dramatically. The weak binding seen for an interlayer channel size <4 Å indicates that the complex becomes less stable due to the pronounced electrostatic repulsive interactions between the positively charged Mg and the negatively charged phosphorene layer. The channel size of 4.84 Å has the most stable binding, corresponding to a 33% volumetric expansion compared to the original black phosphorus crystal. In this case, the binding energy of Mg inserted in bi-layered black phosphorus is −1.366 eV, slightly less than double the binding energy of the monolayer. As shown in Fig. 5c, the distance from the Mg atom to the surface of the top phosphorene layer P1 atom is 2.724 Å, and the distance to the P2/P3 atoms is 2.780 Å. The distance from Mg to the surface of the lower phosphorene layer P4/P5 atoms are 3.388 Å, and P6 is 2.736 Å. The spatial distribution of the charge difference between Mg and black phosphorus is illustrated in Fig. 5d. The large charge deficiency at Mg and charge excess around nearby P atoms indicate that, again, Mg exists in the cationic state. Additionally, we have studied the effect of Mg concentration in Fig. 5b. The absolute value of the binding energy in Mg_xP decreases with increasing x (0 < x <
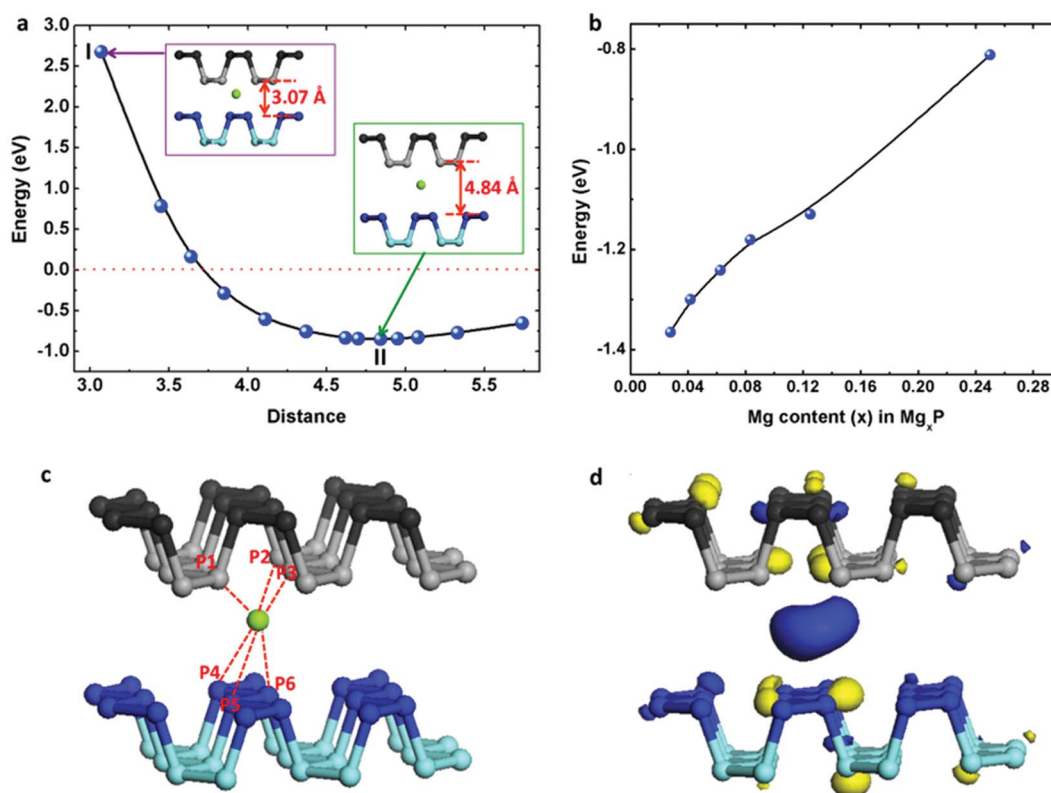
Fig. 5 (a) Total potential energy of Mg inserted into 2-layer phosphorene with respect to phosphorene–phosphorene distance (insert I, Mg inserted with the original channel size of 3.07 Å; insert II, Mg inserted with the most stable channel size of 4.84 Å); (b) binding energies with respect to the Mg concentration; (c) the most stable binding site of Mg inserting onto the 2-layer black phosphorus; (d) charge density difference between Mg and 2-layer black phosphorus.

0.25). For most of the concentrations, Mg has a binding energy lower than -0.8 eV. This indicates the final product of MgP_4 is stable, contributing to a theoretical capacity of 433 mA h g^{-1}.

In addition, we investigate the effect of black phosphorus particle size on Mg insertion. In the primitive cell, the volumetric expansion of 33% requires the crystal overcome a structural stress of 0.062 eV. If one Mg atom can insert in a black phosphorus nanoflake, the area (S) of the nanoflake was evaluated as following,

$$S = -\frac{E_{bind}}{E_{expansion}} \times a \times b \qquad (5)$$

where E_{bind} and $E_{expansion}$ are the binding energy of Mg with both of the upper and lower phosphorene layers, and the binding energy of only two phosphorene layers with a vacuum spacing of 4.84 Å, respectively; a and b are the lattice parameters of black phosphorus. As a consequence, the optimized flake area S for complete intercalation is 3.19 nm², corresponding to a circular flake diameter of 2 nm. Thus, using large sized particles will result in Mg incompletely inserting into black phosphorus.

4. Conclusions

To conclude, our results demonstrate that phosphorene and bulk black phosphorus can store Mg *via* adsorption and

insertion while satisfying the crucial requirement of preserving the P–P bond. Phosphorene and bulk black phosphorus deliver high theoretical capacities of 865 mA h g^{-1} and 433 mA h g^{-1}, respectively, which are double of that of LIBs and SIBs (Table 2). Due to its puckered structure, the diffusion of Mg on phosphorene is highly anisotropic with diffusion along the zigzag direction being highly energetically favorable, while diffusion along the armchair direction is essentially prohibited. The average voltage of the Mg adsorption in phosphorene is estimated to be 0.833 V, suitable for the application as anode in MIBs. We also find that Mg intercalation in bulk black phosphorus is accompanied by a volumetric expansion of 33%. To compensate for the stress of this volumetric expansion, decreasing the particle size can improve the Mg-storage performance.

Table 2 Specific capacities and volumetric expansion of black P and phosphorene anode for Li-, Na-, and Mg-ion batteries, respectively

	Volumetric expansion	Theoretical specific capacity (mA h g^{-1})
Small-size BP to MgP₄	**128%**	**433**
Small-size BP to LiP₄	120%	216
Small-size BP to NaP₄	131%	216
Phosphorene to MgP₂	**290%**	**865**
Phosphorene to LiP₂	238%	433
Phosphorene to NaP₂	310%	433

Conflicts of interest

There are no conflicts to declare.

Acknowledgements

Notes and references

1 R. V. Noorden, *Nature*, 2014, **507**, 26–28.
2 L. Lu, X. Han, J. Li, J. Hua and M. Ouyang, *J. Power Sources*, 2013, **226**, 272–288.
3 J. Tarascon, *Nat. Chem.*, 2010, **2**, 510.
4 Z. Yang, J. Zhang, M. C. Kintner-Meyer, X. Lu, D. Choi, J. P. Lemmon and J. Liu, *Chem. Rev.*, 2011, **111**, 3577–3613.
5 S. W. Kim, D. H. Seo, X. Ma, G. Ceder and K. Kang, *Adv. Energy Mater.*, 2012, **2**, 710–721.
6 V. Palomares, P. Serras, I. Villaluenga, K. B. Hueso, J. Carretero-González and T. Rojo, *Energy Environ. Sci.*, 2012, **5**, 5884–5901.
7 M. D. Slater, D. Kim, E. Lee and C. S. Johnson, *Adv. Funct. Mater.*, 2013, **23**, 947–958.
8 D. Aurbach, Z. Lu, A. Schechter and Y. Gofer, *Nature*, 2000, **407**, 724.
9 D. Aurbach, Y. Gofer, Z. Lu, A. Schechter, O. Chusid, H. Gizbar, Y. Cohen, V. Ashkenazi, M. Moshkovich and R. Turgeman, *J. Power Sources*, 2001, **97**, 28–32.
10 P. Novák, R. Imhof and O. Haas, *Electrochim. Acta*, 1999, **45**, 351–367.
11 C. Pei, F. Xiong, J. Sheng, Y. Yin, S. Tan, D. Wang, C. Han, Q. An and L. Mai, *ACS Appl. Mater. Interfaces*, 2017, **9**, 17060–17066.
12 H. Pan, Y.-S. Hu and L. Chen, *Energy Environ. Sci.*, 2013, **6**, 2338–2360.
13 B. Dunn, H. Kamath and J.-M. Tarascon, *Science*, 2011, **334**, 928–935.
14 W. Xu, J. Wang, F. Ding, X. Chen, E. Nasybulin, Y. Zhang and J.-G. Zhang, *Energy Environ. Sci.*, 2014, **7**, 513–537.
15 G. Zheng, S. W. Lee, Z. Liang, H.-W. Lee, K. Yan, H. Yao, H. Wang, W. Li, S. Chu and Y. Cui, *Nat. Nanotechnol.*, 2014, **9**, 618–623.
16 K. Yan, H.-W. Lee, T. Gao, G. Zheng, H. Yao, H. Wang, Z. Lu, Y. Zhou, Z. Liang and Z. Liu, *Nano Lett.*, 2014, **14**, 6016–6022.
17 N. Sa, T. L. Kinnibrugh, H. Wang, G. Sai Gautam, K. W. Chapman, J. T. Vaughey, B. Key, T. T. Fister, J. W. Freeland and D. L. Proffit, *Chem. Mater.*, 2016, **28**, 2962–2969.
18 N. Wu, Z. Z. Yang, H. R. Yao, Y. X. Yin, L. Gu and Y. G. Guo, *Angew. Chem., Int. Ed.*, 2015, **54**, 5757–5761.
19 L. Wang, K. Asheim, P. E. Vullum, A. M. Svensson and F. Vullum-Bruer, *Chem. Mater.*, 2016, **28**, 6459–6470.
20 J.-S. Kim, W.-S. Chang, R.-H. Kim, D.-Y. Kim, D.-W. Han, K.-H. Lee, S.-S. Lee and S.-G. Doo, *J. Power Sources*, 2015, **273**, 210–215.
21 S. H. Lee, R. A. DiLeo, A. C. Marschilok, K. J. Takeuchi and E. S. Takeuchi, *ECS Electrochem. Lett.*, 2014, **3**, A87–A90.
22 S. Su, Z. Huang, Y. NuLi, F. Tuerxun, J. Yang and J. Wang, *Chem. Commun.*, 2015, **51**, 2641–2644.
23 J. Muldoon, C. B. Bucur, A. G. Oliver, T. Sugimoto, M. Matsui, H. S. Kim, G. D. Allred, J. Zajicek and Y. Kotani, *Energy Environ. Sci.*, 2012, **5**, 5941–5950.
24 Z. Yu, J. Song, M. L. Gordin, R. Yi, D. Tang and D. Wang, *Adv. Sci.*, 2015, **2**, 1400020.
25 J. Sun, G. Zheng, H.-W. Lee, N. Liu, H. Wang, H. Yao, W. Yang and Y. Cui, *Nano Lett.*, 2014, **14**, 4573–4580.
26 C. M. Park and H. J. Sohn, *Adv. Mater.*, 2007, **19**, 2465–2468.
27 W.-C. Chang, K.-W. Tseng and H.-Y. Tuan, *Nano Lett.*, 2017, **17**, 1240–1247.
28 Z. Z. Luo, Y. Zhang, C. Zhang, H. T. Tan, Z. Li, A. Abutaha, X. L. Wu, Q. Xiong, K. A. Khor and K. Hippalgaonkar, *Adv. Energy Mater.*, 2017, **7**, 1601285.
29 J. Song, Z. Yu, M. L. Gordin, S. Hu, R. Yi, D. Tang, T. Walter, M. Regula, D. Choi and X. Li, *Nano Lett.*, 2014, **14**, 6329–6335.
30 Y. Kim, Y. Park, A. Choi, N. S. Choi, J. Kim, J. Lee, J. H. Ryu, S. M. Oh and K. T. Lee, *Adv. Mater.*, 2013, **25**, 3045–3049.
31 W.-J. Li, S.-L. Chou, J.-Z. Wang, H.-K. Liu and S.-X. Dou, *Nano Lett.*, 2013, **13**, 5480–5484.
32 W. Li, S. Hu, X. Luo, Z. Li, X. Sun, M. Li, F. Liu and Y. Yu, *Adv. Mater.*, 2017, **29**, 1605820.
33 J. Sun, H.-W. Lee, M. Pasta, H. Yuan, G. Zheng, Y. Sun, Y. Li and Y. Cui, *Nat. Nanotechnol.*, 2015, **10**, 980–985.
34 J. Sun, H.-W. Lee, M. Pasta, Y. Sun, W. Liu, Y. Li, H. R. Lee, N. Liu and Y. Cui, *Energy Storage Mater.*, 2016, **4**, 130–136.
35 E. S. Reich, *Nature*, 2014, **506**, 19.
36 H. O. Churchill and P. Jarillo-Herrero, *Nat. Nanotechnol.*, 2014, **9**, 330–331.
37 L. D. Chen, J. K. Nørskov and A. C. Luntz, *J. Phys. Chem. C*, 2015, **119**, 19660–19667.
38 L. F. Wan and D. Prendergast, *J. Phys. Chem. C*, 2018, **122**, 398–405.
39 P. Canepa, S.-H. Bo, G. S. Gautam, B. Key, W. D. Richards, T. Shi, Y. Tian, Y. Wang, J. Li and G. Ceder, *Nat. Commun.*, 2017, **8**, 1759.
40 C. Zhang, M. Shao, F. Ning, S. Xu, Z. Li, M. Wei, D. G. Evans and X. Duan, *Nano Energy*, 2015, **12**, 231–239.
41 S.-T. Zhang, H. Yan, M. Wei, D. G. Evans and X. Duan, *J. Phys. Chem. C*, 2012, **116**, 3421–3431.

42 Z. Wang, Q. Su, J. Shi, H. Deng, G. Q. Yin, J. Guan, M. P. Wu, Y. L. Zhou, H. L. Lou and Y. Q. Fu, *ACS Appl. Mater. Interfaces*, 2014, **6**, 6786–6789.

43 C. Zhang, M. Yu, G. Anderson, R. R. Dharmasena and G. Sumanasekera, *Nanotechnology*, 2017, **28**, 075401.

44 W. Li, Y. Yang, G. Zhang and Y.-W. Zhang, *Nano Lett.*, 2015, **15**, 1691–1697.

45 O. I. Malyi, T. L. Tan and S. Manzhos, *J. Power Sources*, 2013, **233**, 341–345.

46 K. Hembram, H. Jung, B. C. Yeo, S. J. Pai, S. Kim, K.-R. Lee and S. S. Han, *J. Phys. Chem. C*, 2015, **119**, 15041–15046.